Smart Materials and Structures

PAPER

A phase evolution based constitutive model for shape memory polymer and its application in 4D printing

To cite this article: Fangfang Wang *et al* 2020 *Smart Mater. Struct.* **29** 055016

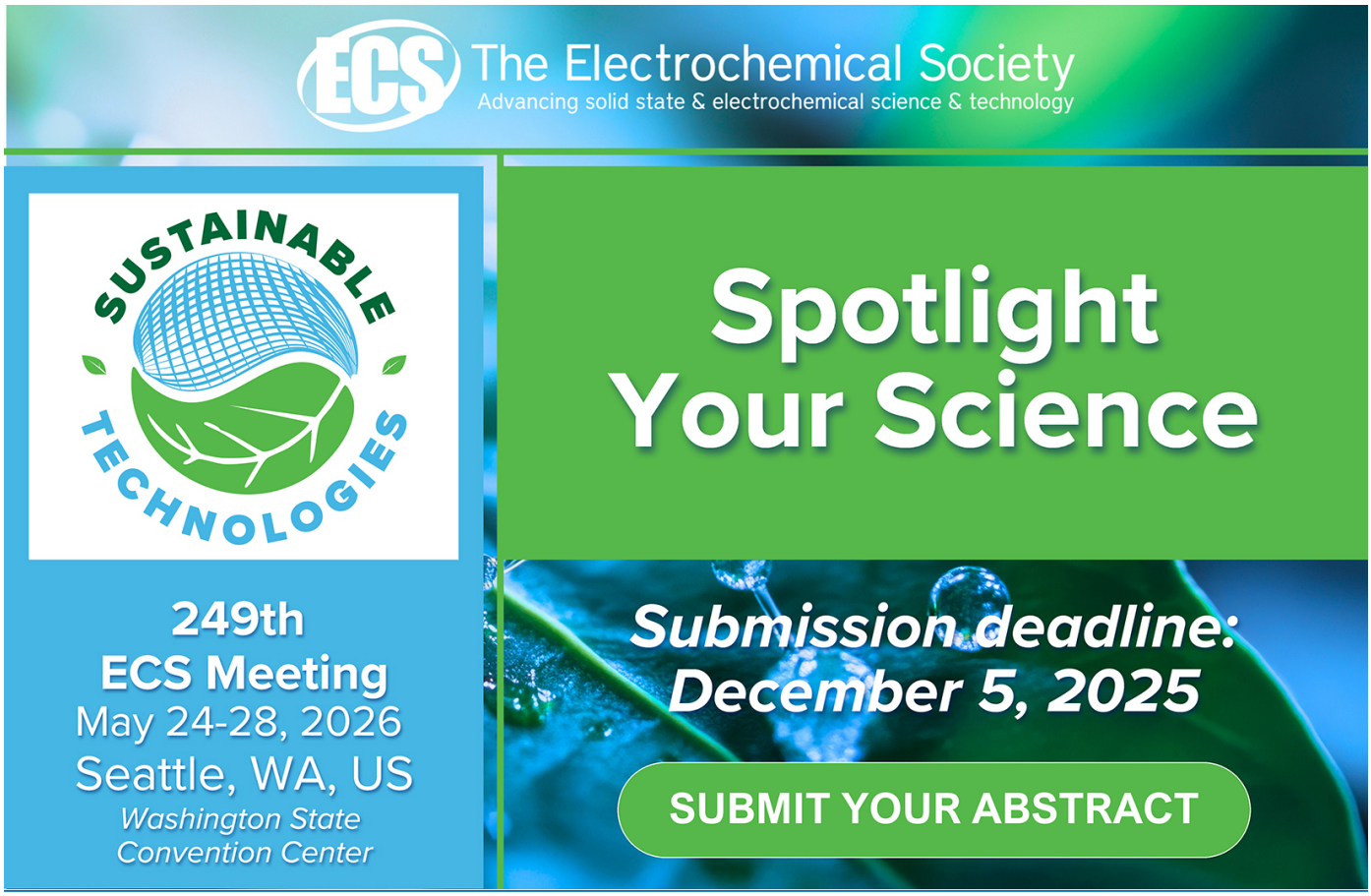

IOP Publishing Smart Materials and Structures
Smart Mater. Struct. 29 (2020) 055016 (14pp) https://doi.org/10.1088/1361-665X/ab7ab0

A phase evolution based constitutive model for shape memory polymer and its application in 4D printing

Fangfang Wang[1,2,6], Chao Yuan[1,6], Dong Wang[3], David W Rosen[1,4] and Qi Ge[1,5]

[1] Digital Manufacturing and Design Centre, Singapore University of Technology and Design, Singapore 487372, Singapore
[2] School of Civil Engineering, Xi'an University of Technology, Xi'an 710048, People's Republic of China
[3] School of Mechanical Engineering, Shanghai Jiao Tong University, Shanghai 200241, People's Republic of China
[4] The G. W. Woodruff School of Mechanical Engineering, Georgia Institute of Technology, Atlanta, GA 30332, United States of America
[5] Department of Mechanical and Energy Engineering, Southern University of Science and Technology, Shenzhen 518055, People's Republic of China

E-mail: geq@sustech.edu.cn

Received 14 October 2019, revised 16 February 2020
Accepted for publication 27 February 2020
Published 31 March 2020

Abstract

4D printing is a novel concept and multidiscipline research area which integrates advanced manufacturing, material science and mechanics. As an active material with high stiffness and rapid response speed, shape memory polymer (SMP) is widely used in 4D printing structures. Accordingly, a simple but effective theoretical model becomes highly desirable to better assist the 4D printing design. In this paper, a phenomenological model is developed in which the concept of phase evolution is used to describe the glass transition behavior of SMP. Explicit iterative format has been derived where the stress–strain behaviors of phase generation and phase vanishment are distinguished. The model is further employed to predict the shape memory behavior of pure SMP and active bending behavior of SMP-elastomer bilayer composites. With its inherent conciseness and generality, the model is promising to be applicable in modelling other soft active materials with phase evolution behaviors.

Supplementary material for this article is available online

Keywords: 4D printing, shape memory polymer, phase evolution, constitutive model

(Some figures may appear in colour only in the online journal)

1. Introduction

4D printing [1–3] has become a vibrant and attractive research area which combines the knowledge of manufacturing, material science and mechanics. This innovative concept aims to endow the 3D printed objects with the capability of shape transformation from as-printed shape to predesigned target shape over the fourth dimension—'time'. The key factor of realizing 4D printing is the cooperation between active materials and shape-morphing mechanism. During the past few years, novel 4D printing designs with different active materials [4–7] and mechanisms [8–15] have been reported. Among them, shape memory polymer (SMP) [3, 6–8, 11, 13, 14, 16, 17] is one of the most widely used active materials due to its relatively high modulus and quick response [18, 19].

During a typical shape memory (SM) cycle, an SMP sample is firstly deformed from its original shape at a high

[6] These two authors contributed equally to this work.

temperature which is above its transition temperature (glass transition temperature T_g [20, 21] or melting transition temperature T_m [22, 23]) followed by being cooled to a low temperature below the transition temperature while the external constraint is maintained. Upon releasing the external constraint at the low temperature, most of the deformed shape is retained due to the highly reduced mobility of the polymer chains. This fixed shape is referred to as the temporary shape. The temperature-responsive shape shifting which is commonly observed in 4D printing demonstrations occurs in the final step of a SM cycle where the SMP sample recovers to its original shape from the temporary shape upon being reheated above the transition temperature again [24–26].

To better assist the utilization of SMP in the field of 4D printing, the aforementioned SM behavior should be well described by proper theoretical model. Among the existing constitutive models of SMP, two categories have been widely adopted: the thermoviscoelasticity based models [20, 21, 27–32] and the phase evolution based models [22, 33–38]. For the former one, SMP is considered as a viscoelastic material and its time-temperature dependent viscoelastic behavior can be described by the constitutive models that consist of the spring-dashpot constructed Maxwell elements. In these models, the deformation of the dashpot incurred at high temperature is almost fixed at low temperature since the relaxation time is extended from less than a second to a few months and even years [20, 21] so that the dashpot becomes too viscous to deform. It has been evident that the thermoviscoelasticity based models can well capture the time-dependent or temperature-dependent response of the SMP in a SM cycle. However, the thermoviscoelastic model requires a great number of material parameters and the parameter-fitting process is relative complicated and laboursome. Although researchers have developed the significantly simplified models [17, 21, 27, 31] by using the linear Maxwell elements to ignore the nonlinear effect [28, 30], it is still challenging and computationally inefficient to implement the viscoelastic based constitutive models into complex geometries for the design of 4D printing structures. In contrast, the constitutive models based on phase evolution approach phenomenologically treat SMP as a multiphase mixture in which different phases (i.e. rubbery/glassy phases in amorphous SMPs, and crystalline/melting phases in semi-crystalline SMPs) could mutually transform upon temperature variation. Besides the capability of predicting SM effect, the phase evolution based models could also be able to capture the nonlinear stress–strain behaviors of SMPs by implementing complicated equations of hyperelasticity and viscoplasticity [36].

However, in many applications of 4D printing [3, 8, 11, 39], compared to the time-dependent shape evolution, designers are more interested in how to achieve desired target shape through material modeling and structure design. Therefore, a simplified constitutive model of SMP that can capture the modulus change over temperature and predict the shape fixing behavior is sufficient for most 4D printing designs . In addition, it is favorable if the simplified constitutive model is easily understandable to the designers, and the model can be readily implemented into 4D printing designs with complex geometries.

In this paper, we report such a simplified phenomenological model based on the phase evolution concept for 4D printing designers. In this model, the required material parameters can be directly determined from some basic material tests without further curve fitting, and explicit solutions can be derived to predict the SM effect. Furthermore, due to its conciseness, the model can be incorporated into specific structures without obvious difficulty. The paper is organized as follows. In section 2, the fabrication, basic characterization and SM experiment for pure SMP is reported. In section 3, the general iterative format for the constitutive model is derived. In section 4, the analytical solutions for the SM behavior of pure SMP under stress control and strain control modes are respectively given. In section 5, the model is further employed to predict the active bending behavior of the SMP-elastomer bilayer composites. In sections 6 and 7, some discussion and concluding remarks are respectively given.

2. Experiment

2.1. Materials and fabrication

In this work, two commercial photopolymers Vero and Tango are used for polyjet 3D printing. Vero is a rigid material with glass transition temperature about 60 °C, and therefore used as SMP. Tango behaves like an elastomer and is used to construct active composites together with Vero.

All the test samples are fabricated on a commercial polyjet 3D printer (Objet500 Connex3, Stratasys, Edina, MN, USA) which works by ultraviolet (UV) curing the wiped photopolymer droplets deposited from the print heads in a layer-by-layer manner.

Herein, it should be noted that based on the previous study [8, 40], the residual stress during polyjet 3D printing may affect the final bending curvature of the bilayer composites where a longer layer printing time may embed a higher compression strain in the elastomer layer, and accordingly yield a greater strain mismatch upon heating. In order to avoid the side effect induced by the residual stress during the printing process, our samples were printed with a layer printing time of 8 s. From the experimental quantifications from the aforementioned article [8], the built-in strain in the elastomer layer is neglectable when the layer printing time is below 10 s.

2.2. Thermomechanical characterizations

In order to characterize the thermomechanical properties of the materials and identify the parameters used in the theoretical model, dynamic mechanical analysis (DMA), thermal expansion tests and uniaxial tensile tests were conducted on a dynamic mechanical analyzer (Model Q800, TA Instruments, New Castle, DE, USA). All the test samples were designed with a dimension of 15 mm × 3 mm × 0.5 mm.

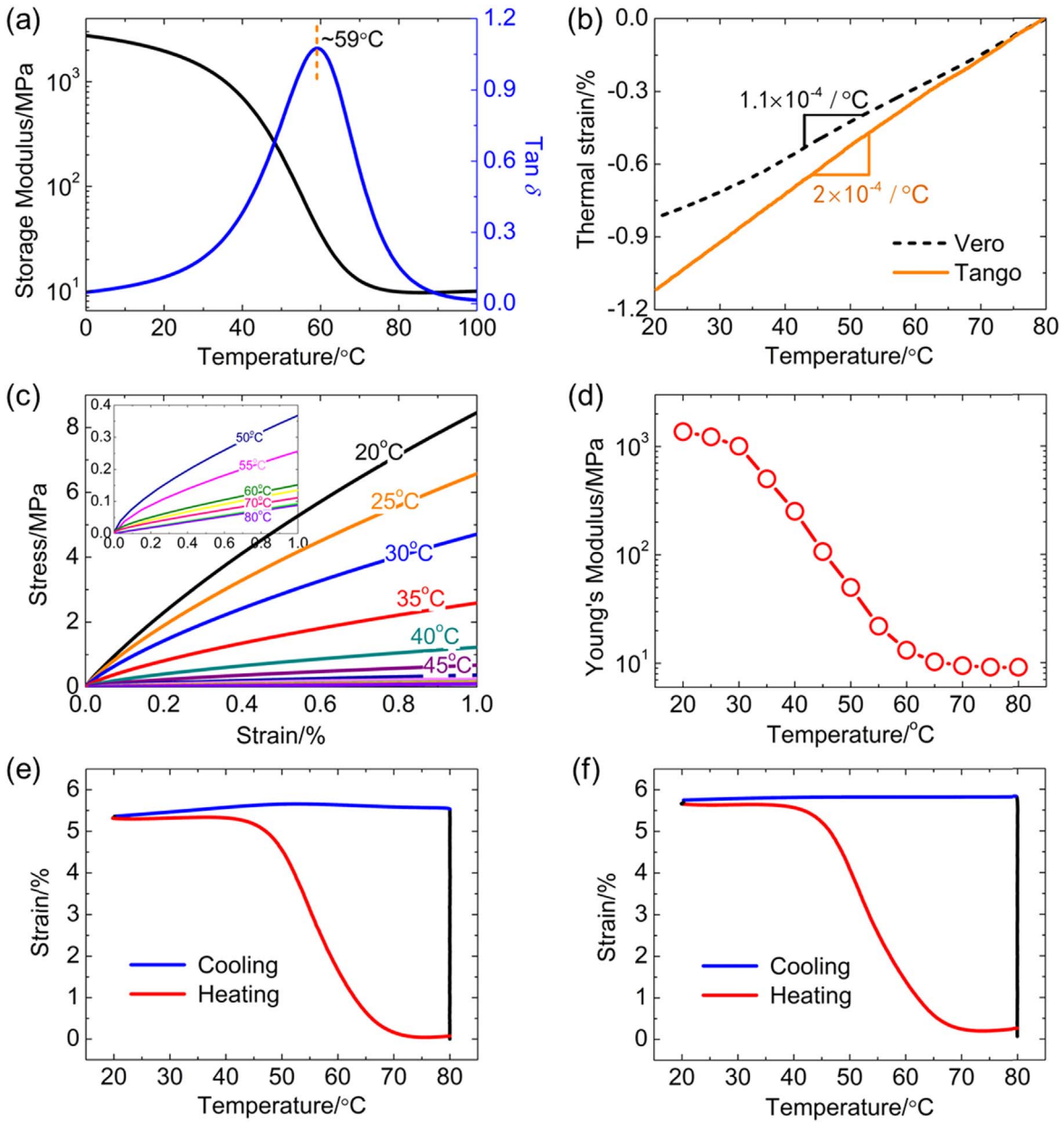

Figure 1. Thermomechanical characterizations and SM behaviors of 3D printed photopolymers. (a) Temperature dependence of storage modulus and loss factor (tanδ) of Vero. (b) Temperature dependence of thermal strain of Vero and Tango. (c) Uniaxial tension curves of Vero at elevated temperatures. (d) Temperature dependence of Young's modulus of Vero. (e) SM behavior of Vero under stress control mode. (f) SM behavior of Vero under strain control mode.

For the DMA test, a sample was initially equilibrated at 100 °C for 15 min under a preload of 1 mN. Then an oscillatory strain with a frequency of 1 Hz and amplitude of 0.1% was applied to the sample and the temperature was linearly ramped down from 100 °C to 0 °C at a rate of 2 °C min^{-1}. As shown in figure 1(a), the storage modulus and loss factor (tanδ) of Vero were recorded as a function of temperature. The glass transition temperature (T_g) was identified to be 59 °C which corresponds to the peak of the tanδ curve.

Thermal expansion tests of Vero and Tango were respectively performed under the controlled force mode where a preload of 1 mN was maintained to prevent the sample from buckling. The samples were first equilibrated at 80 °C for 15 min followed by being cooled from 80 °C to 20 °C at a rate of 2 °C min^{-1}. As shown in figure 1(b), the coefficients of thermal expansion (CTEs) of Vero and Tango were determined to be 1.1×10^{-4} °C^{-1} and 2.0×10^{-4} °C^{-1} from the tangent of their respective thermal strain-temperature curves.

Uniaxial tensile tests of Vero were conducted at elevated temperatures ranging from 20 °C to 80 °C with an interval of 5 °C. The sample was first equilibrated at a predefined temperature for 15 min followed by being loaded at a rate of 6 N min^{-1}. Young's modulus was determined from the tangent of the stress–strain curve. The stress–strain curves and temperature dependence of Young's modulus are respectively shown in figures 1(c) and (d).

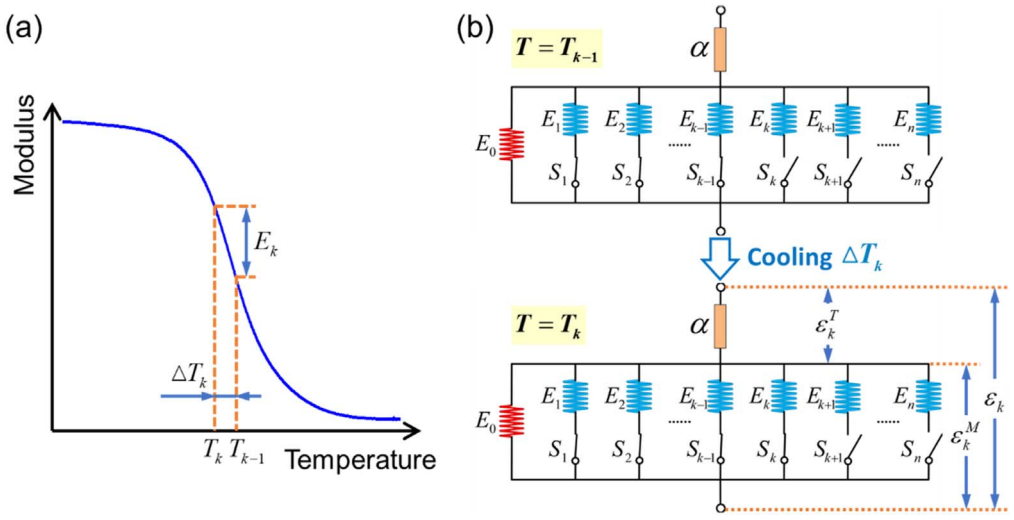

Figure 2. (a) Variation of modulus with temperature during the glass transition process. (b) Schematic diagram of the phase evolution model.

2.3. Shape memory behavior of pure SMP

Shape memory behavior of pure SMP was tested under two types of programming methods, which were respectively denoted as stress control mode and strain control mode.

For the stress control mode, the sample was first equilibrated at 80 °C for 15 min followed by being loaded at a rate of 0.5 MPa min^{-1}. Upon reaching 0.5 MPa, the stress was maintained while the temperature was decreased from 80 °C to 20 °C at a rate of 2 °C min^{-1}. After the sample was cooled to 20 °C, the temporary shape was obtained by releasing the external stress. Finally, the free recovery was realized by heating the sample from 20 °C to 80 °C at a rate of 2 °C min^{-1}.

Distinguished from the stress control mode, strain control mode started by stretching the sample by 6% at a strain rate of 6%/min. Then the sample was cooled from 80 °C to 20 °C at a rate of 2 °C min^{-1} while the strain was maintained. Besides, there was no difference between the stress control mode and strain control mode.

The strain variations under the two programming modes within a SM cycle were respectively shown in figures 1(e) and (f). For the stress control mode shown in figure 1(e), the strain in the cooling step slightly varies due to the combined effect of thermal expansion and entropic elasticity. For the strain control mode shown in figure 1(f), the strain in the cooling step keeps constant due to the external constraint. However, despite of the programming mode, good shape fixity and shape recovery are both achievable.

3. Constitutive model

3.1. Basic considerations

For a typical amorphous SMP, the SM programming is performed within a temperature range where glass transition occurs. As shown in figure 2(a), the modulus of SMP varies significantly during glass transition where the evolution between rubbery phase and glassy phase takes place in the material.

To describe the mechanical behavior during glass transition, a phenomenological constitutive model is developed where multiple branches of springs and switches are employed with a parallel arrangement. As shown in figure 2(b), a thermal expansion component with CTE α is connected in series with the parallel branches to describe the effect of linear thermal expansion. Therefore, the total strain of the material is the sum of mechanical strain and thermal strain

$$\varepsilon = \varepsilon^M + \varepsilon^T. \tag{1}$$

For the parallel branches, in addition to the leftmost branch with a single spring whose spring constant E_0 represents the rubbery modulus of SMP, the remaining branches are composed of a spring in series with a temperature-controlled switch. During the cooling process, the temperature-controlled switches successively turn on to simulate the generation of new glassy phases, which corresponds to the increase of modulus. Likewise, when the temperature increases, the switches may sequentially turn off to simulate the vanishment of existing glassy phases, giving rise to the decline of modulus.

For a general branch, $E_k (k = 1, 2, \cdots, n)$ represents the modulus of the kth glassy phase generated at temperature T_k during glass transition, and the switch S_k maintains disconnected when the temperature is above T_k. Once the temperature decreases below T_k, the switch S_k turns on.

From the physical point of view, the kth glassy phase generates after the $(k-1)$th glassy phase during the cooling process and vanishes prior to the $(k-1)$th glassy phase during heating. It is assumed that the kth glassy phase does not carry load (stress-free) when it is newly formed. After its generation, the kth glassy phase starts to carry load and deform until its vanishing when S_k turns off. Therefore, at temperature $T = T_k$, there are totally k glassy phases $(0 \leqslant k \leqslant n)$ formed and the temporary elastic modulus of the

material is

$$E(T_k) = \sum_{i=0}^{k} E_i. \tag{2}$$

3.2. Constitutive equations

Generally, two typical scenarios may occur in the phase evolution of SMP: formation of new glassy phase or vanishment of existing glassy phase. In this section, constitutive equations are respectively derived.

3.2.1. Formation of new glassy phase. Consider a state where $k-1$ glassy phases exist at temperature T_{k-1}. As shown in figure 2(b), since the branches labelled from 1 to $k-1$ are all connected, the total stress is calculated by

$$\sigma_{k-1} = \sum_{i=0}^{k-1} E_i \varepsilon_{i,k-1}^{M}, \tag{3}$$

where $\varepsilon_{i,k-1}^{M}$ denotes the mechanical strain of the ith branch at the $(k-1)$th increment.

After a temperature increment $\triangle T_k$ ($\triangle T_k < 0$), the kth glassy phase is generated and starts to carry load (figure 2(b)). Accordingly, the total stress is updated and denoted as

$$\sigma_k = \sum_{i=0}^{k} E_i \varepsilon_{i,k}^{M}. \tag{4}$$

Since all the branches are parallelly arranged, after the temperature increment ΔT_k, all the connected branches ($E_0 \sim E_k$) undergo the same mechanical deformation increment $\triangle \varepsilon_k^M$, which is equal to the current mechanical strain in the newly generated kth glassy phase. Therefore, by subtracting equation (3) from equation (4), we have the stress increment corresponding to the temperature increment ΔT_k as

$$\triangle \sigma_k = E(T_k) \ \triangle \ \varepsilon_k^M, \tag{5}$$

where $E(T_k)$ is the temporary elastic modulus at temperature T_k as given by equation (2).

Substituting equation (1) into (5) and considering the linear thermal expansion relation $\triangle \varepsilon_k^T = \alpha \triangle T_k$, we have the general iterative format to describe the stress increment when a new glassy phase is generated at temperature T_k

$$\triangle \sigma_k = E(T_k)(\triangle \varepsilon_k - \alpha \triangle T_k). \tag{6}$$

3.2.2. Vanishment of existing glassy phase. In order to analyze the vanishment of existing glassy phase, for convenience, we assume an initial state where all the glassy branches are connected. Then we consider a general case where $k+1$ glassy branches labelled from 1 to $k+1$ are connected at temperature T_{k+1}. Since there are $n-(k+1)$ disconnected switches, we specify the current increment number is $n-k-1$, and the corresponding total stress is

$$\sigma_{n-k-1} = \sum_{i=0}^{k+1} E_i \varepsilon_{i,n-k-1}^{M}, \tag{7}$$

where $\varepsilon_{i,n-k-1}^{M}$ denotes the mechanical strain of the ith branch at increment $n-k-1$.

When the temperature increases to T_k (increment $n-k$), the originally existed $(k+1)$th glassy phase vanishes, hence the corresponding stress is updated as

$$\sigma_{n-k} = \sum_{i=0}^{k} E_i \varepsilon_{i,n-k}^{M}. \tag{8}$$

Similar to the derivation in section 3.2.1, after the temperature increment, all the connected branches ($E_0 \sim E_k$) undergo the same mechanical deformation increment $\triangle \varepsilon_{n-k}^M$. Therefore, the subtraction of equation (7) from (8) yields the stress increment as

$$\triangle \sigma_{n-k} = E(T_k) \ \triangle \ \varepsilon_{n-k}^{M} - E_{k+1} \varepsilon_{k+1,n-k-1}^{M}, \tag{9}$$

where $E(T_k)$ is the temporary elastic modulus at temperature T_k as given by equation (2).

Herein, it should be noted that equation (9) is not as concise as equation (5) since the existence of the second term $E_{k+1}\varepsilon_{k+1,n-k-1}^{M}$ which relates to the mechanical strain of the $(k+1)$th branch at the $(n-k-1)$th increment during the process of phase vanishing. However, this term can be further simplified when the model is employed to analyze a SM cycle. Based on our basic considerations given in section 3.1, the $(k+1)$th glassy branch begins to deform after the kth increment in the phase formation process when the mechanical strain of the material is $\varepsilon_k^{M,C}$. Herein, the superscript 'C' represents cooling. Therefore, we have

$$\varepsilon_{k+1,n-k-1}^{M} = \varepsilon_{n-k-1}^{M} - \varepsilon_k^{M,C}, \tag{10}$$

where ε_{n-k-1}^{M} represents the mechanical strain of the material at the $(n-k-1)$th increment during the process of phase vanishing.

Upon substituting equation (10) into equation (9), we have the simplified form of the stress increment during the phase vanishing process

$$\triangle \sigma_{n-k} = E(T_k) \ \triangle \ \varepsilon_{n-k}^{M} - E_{k+1}(\varepsilon_{n-k-1}^{M} - \varepsilon_k^{M,C}). \tag{11}$$

Substituting equation (1) into equation (11) and considering the linear thermal expansion relation, we have the general iterative format to describe the stress increment when existing glassy phase is vanished

$$\triangle \sigma_{n-k} = E(T_k) \ \triangle \ \varepsilon_{n-k} - E_{k+1}\varepsilon_{n-k-1} + E_{k+1}\varepsilon_k^C + E(T_{k+1})\alpha \triangle T_{k+1}. \tag{12}$$

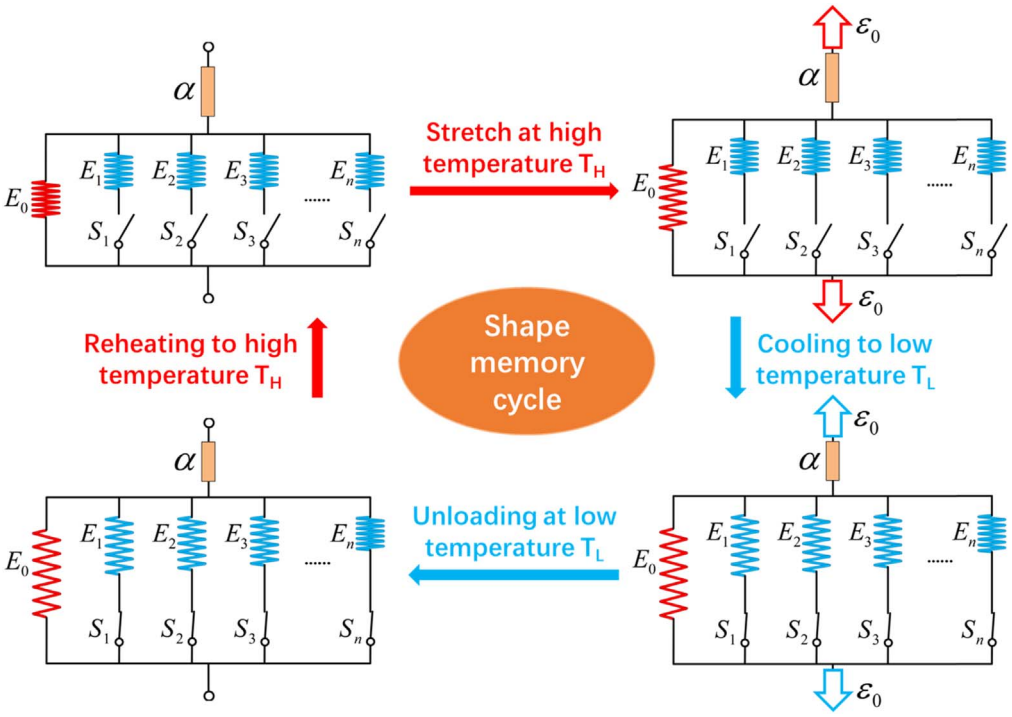

Figure 3. Shape memory behavior under uniaxial tension of strain control mode.

4. Shape memory behavior of pure SMP under uniaxial loading

In this section, the phase evolution model is employed to analyze the SM behavior of SMP under uniaxial loading. Figure 3 illustrates the phase evolution process in a typical SM cycle. The material is first stretched at high temperature T_H where no glassy phase is formed to share the external load. Then the material is cooled from T_H to a low temperature T_L while the external load is maintained. During the cooling process, new glassy phase is successively formed until the material is in a fully glassy state at T_L where all the n glassy branches are connected. Upon releasing the external load at T_L, the stresses in all the glassy phases are redistributed to satisfy the equilibrium of internal force. As a consequence, a temporary shape is fixed in the material. Finally, the material is reheated to the high temperature T_H where all the glassy phases vanish again to render the shape recovery. It should be noted that since the SM response is affected by the loading method, the analytical solutions of the stress–strain response under stress control and strain control are respectively derived. For more details regarding the derivation of the equations in this section, please refer to the supplementary materials is available online at stacks.iop.org/SMS/29/055016/mmedia.

4.1. Stress control

Upon applying a constant stress σ_0 at high temperature T_H, only the rubbery phase is deformed to compensate the external loading. Since the thermal strain at T_H is defined as 0, the total strain ε is equal to the mechanical strain ε^M

$$\varepsilon = \varepsilon^M = \frac{\sigma_0}{E_0}. \tag{13}$$

In the cooling process, the total stress remains σ_0. Based on equation (6), we can obtain the total strain ε at an intermediate temperature T_k ($T_L \leqslant T_k \leqslant T_H$)

$$\varepsilon(T_k) = \frac{\sigma_0}{E_0} + \alpha(T_k - T_H). \tag{14}$$

After releasing the load at T_L, according to equation (6), the stress decrementation $\triangle\sigma = -\sigma_0$ leads to an updated total strain

$$\varepsilon = \frac{\sigma_0}{E_0} + \alpha(T_L - T_H) - \frac{\sigma_0}{E(T_L)}. \tag{15}$$

Normally, the glassy modulus $E(T_L)$ of an SMP is 2 orders of magnitude greater than its rubbery modulus E_0. So compared with the initial strain σ_0/E_0, the strain variation $\sigma_0/E(T_L)$ upon unloading is negligible, which reveals the fixity of the temporary shape.

For the reheating process, the stress remains 0. According to equations (12), (14) and (15), we can obtain the strain at an intermediate temperature T_k ($T_L \leqslant T_k \leqslant T_H$)

$$\varepsilon(T_k) = \frac{\sigma_0}{E_0} + \alpha(T_k - T_H) - \frac{\sigma_0}{E(T_k)}. \tag{16}$$

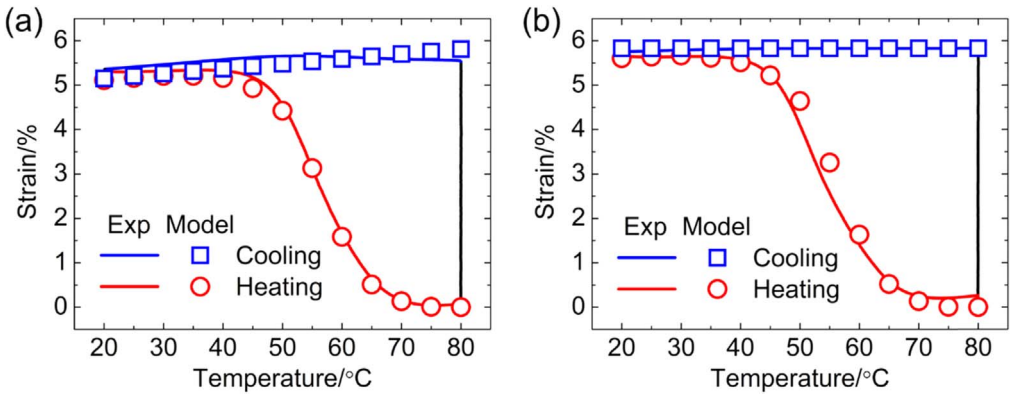

Figure 4. Relationship between strain and temperature during the shape memory cycle. (a) The stress control mode, (b) The strain control mode.

Particularly, when the SMP is reheated to T_H, the total strain $\varepsilon(T_H)$ equals to 0, which indicates the full recovery from temporary shape to initial shape.

4.2. Strain control

For the case of strain control, a constant strain ε_0 is first applied on the SMP at T_H, which yields the total stress

$$\sigma = E_0\varepsilon_0. \tag{17}$$

Since the strain is maintained within the entire cooling step, based on equation (6), the stress at an intermediate temperature T_k ($T_L \leqslant T_k \leqslant T_H$) is

$$\sigma(T_k) = E_0\varepsilon_0 + \alpha\sum_{i=1}^{k}[E(T_i)(T_{i-1} - T_i)]. \tag{18}$$

After releasing the constraint at T_L, the total stress becomes 0, the corresponding strain can be obtained based on equations (6) and (18)

$$\varepsilon = \varepsilon_0 - \frac{E_0\varepsilon_0}{E(T_L)} + \alpha\frac{\sum_{i=1}^{n}[E(T_i)(T_i - T_{i-1})]}{E(T_L)}. \tag{19}$$

Upon reheating from T_L to T_H, the strain varies with the temperature under the stress-free state. For an intermediate temperature T_k, based on equations (12) and (19), we can obtain

$$\varepsilon(T_k) = \varepsilon_0 - \frac{E_0\varepsilon_0}{E(T_k)} + \alpha\frac{\sum_{i=1}^{k}[E(T_i)(T_i - T_{i-1})]}{E(T_k)}. \tag{20}$$

Similar to the case of stress control, equation (20) indicates a full shape recovery at T_H where the total strain $\varepsilon(T_H) = 0$.

4.3. Theoretical predictions

In order to employ the above equations to predict the SM behavior of SMP, model parameters should be determined based on the material characterization tests. The spring constant in each branch is equal to the increment of Young's modulus at the corresponding temperature. According to figure 1(d), we divide the programming temperature range (20 °C–80 °C) into 12 increments. Therefore, one rubbery phase branch and 12 temperature-controlled glassy phase branches are used in the following theoretical predictions. The detailed spring constant parameters are listed in table 1. Herein, it should be noted that the number of branches will not affect the modelling results. More details regarding the effect of branch number could be found in the supplementary materials.

Table 1. Spring constant parameters for the constitutive model.

Branch number k	Spring constant E_k(MPa)	Branch number k	Spring constant E_k(MPa)
0	9.1	7	57
1	0.1	8	145
2	0.3	9	250
3	0.8	10	504
4	2.9	11	219
5	8.8	12	143
6	28		

With the identified model parameters, the relationship between strain and temperature under two different programming modes are respectively predicted. As shown in figures 4(a) and (b), good agreement has been achieved between the theoretical predictions and experimental results, which validates the efficiency of the phase evolution model.

5. Bending of active composites

5.1. Analytical solution

Upon accurately predicting the SM behavior of pure SMP, we further implement SMP into composite structures and employ the phase evolution model to analyze the bending of active composites.

Figure 5(a) shows the schematic of active composite (length L, height h and width w) where two SMP/elastomer laminates are alternatively connected along the length direction with their respective segment lengths (L_1, L_2) and thicknesses of SMP layers (h_S^I, h_S^{II}) and elastomer layers (h_E^I,

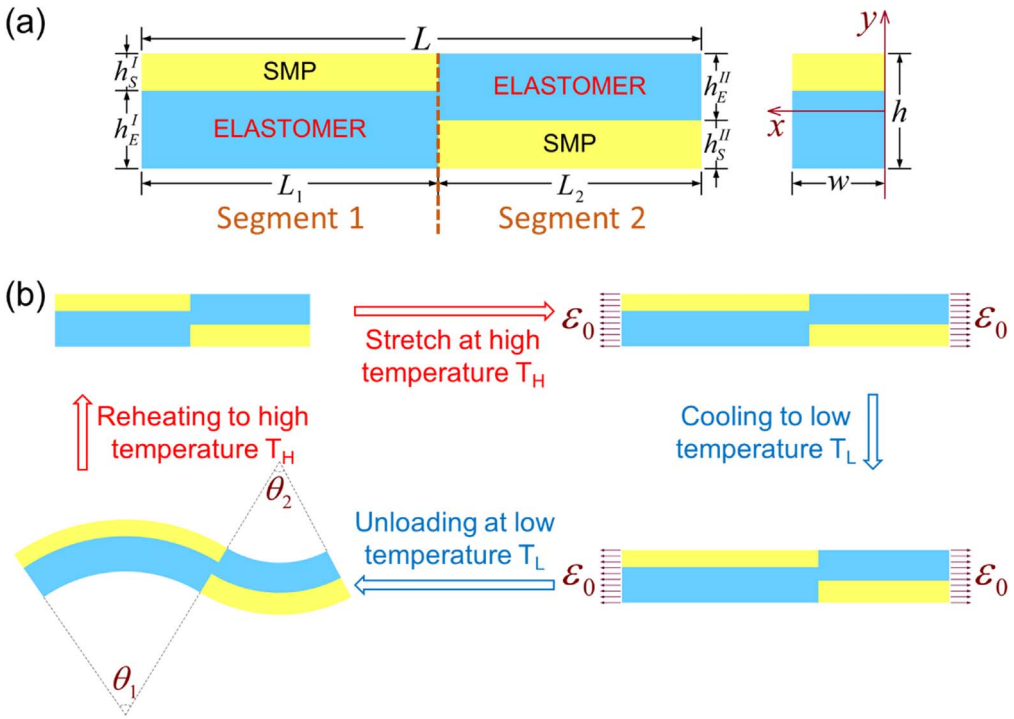

Figure 5. (a) Schematic of a double bilayer shape memory composites (b) shape memory programming of a double bilayer shape memory composites under uniaxial strain loading.

h_E^{II}). Herein, we use the superscripts '*I*' and '*II*' to denote the segment number and subscripts '*S*' and '*E*' to denote the SMP and elastomer layers.

Similar to the thermomechanical programming of pure SMP, we first stretch the active composite uniaxially to an initial strain ε_0 at high temperature T_H followed by cooling it to the low temperature T_L while maintaining the strain (figure 5(b)).

Upon releasing external constraint at T_L, the SMP layers manage to maintain the current configuration whereas the elastomer layers are prone to recover the undeformed shape. As a result, the composite may bend to accommodate the mismatch strain. However, once the strain mismatch is reduced by increasing the temperature to T_H, the composite recovers to its initial shape.

For the first step, since the magnitudes of the rubbery modulus between SMP and elastomer are relatively close, it is reasonable to assume that the SMP and elastomer layers in the same segment are equally stretched. Moreover, since the stiffness differs between segments, the strains of segment 1 and 2 are different and respectively calculated by $\varepsilon_0^I = \Delta L_1/L_1$ and $\varepsilon_0^{II} = \Delta L_2/L_2$, where ΔL_1 and ΔL_2 are the elongations of segment 1 and 2. To accommodate the strain compatibility, the total elongation of the composite is obtained by

$$\Delta L = \Delta L_1 + \Delta L_2. \tag{21}$$

Consider the force balance at the segment interface, we have

$$\sigma_{S,0}^I \cdot h_S^I + \sigma_{E,0}^I \cdot h_E^I = \sigma_{S,0}^{II} \cdot h_S^{II} + \sigma_{E,0}^{II} \cdot h_E^{II}, \tag{22}$$

where $\sigma_{S,0}^{I/II}$ and $\sigma_{E,0}^{I/II}$ denote the stresses in the SMP and elastomer layers at T_H and can be calculated by

$$\sigma_{S,0}^{I/II} = E_S(T_H) \cdot \varepsilon_0^{I/II} \text{ and } \sigma_{E,0}^{I/II} = E_E \cdot \varepsilon_0^{I/II}, \tag{23}$$

where E_E and E_S respectively denote the modulus of the elastomer and SMP material.

Combining equations (21)–(23), segment strain ε_0^I and ε_0^{II} are solved as

$$\varepsilon_0^I = \frac{\varepsilon_0 L[E_E h_E^{II} + E_S(T_H) \cdot h_S^{II}]}{L_1[E_E h_E^{II} + E_S(T_H) \cdot h_S^{II}] + L_2[E_E h_E^I + E_S(T_H) \cdot h_S^I]}, \tag{24}$$

and

$$\varepsilon_0^{II} = \frac{\varepsilon_0 L[E_E h_E^I + E_S(T_H) \cdot h_S^I]}{L_1[E_E h_E^{II} + E_S(T_H) \cdot h_S^{II}] + L_2[E_E h_E^I + E_S(T_H) \cdot h_S^I]}. \tag{25}$$

For the second step, based on equations (6) and (23), the stresses in the SMP layer and elastomer layer at an intermediate temperature T_k ($T_L \leqslant T_k \leqslant T_H$) are

$$\sigma_S^{I/II}(T_k) = E_S(T_H) \cdot \varepsilon_0^{I/II} + \sum_{i=1}^{k} [E_S(T_i)(\Delta\varepsilon_i^{I/II} - \alpha_S \Delta T_i)], \tag{26}$$

and

$$\sigma_E^{I/II}(T_k) = E_E \cdot \varepsilon_0^{I/II} + E_E \sum_{i=1}^{k} (\Delta\varepsilon_i^{I/II} - \alpha_E \Delta T_i), \tag{27}$$

where $\Delta\varepsilon_i^{I/II}$ denotes the total strain increment of segment 1 or 2 in response to a temperature increment ΔT_i and $\alpha_{S/E}$ is the CTE. The total strain increment $\Delta\varepsilon_i^I$ and $\Delta\varepsilon_i^{II}$ in equations (26) and (27) can be obtained by accommodating

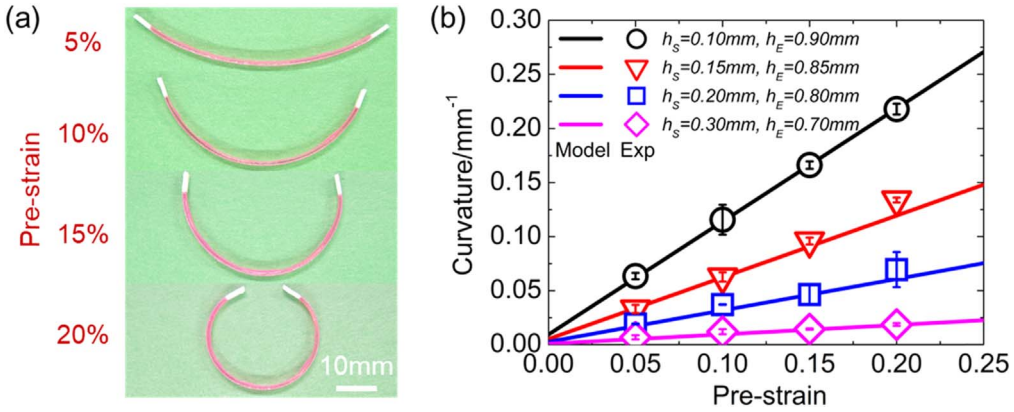

Figure 6. (a) Bending configurations of bilayer laminates (dimension: 60 mm × 5 mm × 1 mm) under elevated initial strain. The thickness ratio of SMP and elastomer is 1:4. (b) Theoretical predictions and experimental results of the bending curvature under elevated initial strain and different thickness ratios of SMP and elastomer.

the strain compatibility and force balance as

$$\triangle\varepsilon_i^I = \frac{L_2\triangle T_i[\alpha_E E_E(h_E^I - h_E^{II}) + \alpha_S E_S(T_i)(h_S^I - h_S^{II})]}{L_1[E_S(T_i)h_S^{II} + E_E h_E^{II}] + L_2[E_S(T_i)h_S^I + E_E h_E^I]}, \tag{28}$$

and

$$\triangle\varepsilon_i^{II} = \frac{L_1\triangle T_i[\alpha_E E_E(h_E^{II} - h_E^I) + \alpha_S E_S(T_i)(h_S^{II} - h_S^I)]}{L_1[E_S(T_i)h_S^{II} + E_E h_E^{II}] + L_2[E_S(T_i)h_S^I + E_E h_E^I]}. \tag{29}$$

After releasing the constraint at T_L, the composite bends into an '*S*' shape where segment 1 and 2 exhibit their respective curvatures κ^I and κ^{II}. For segment 1, denote the mid-plane ($y = 0$) strain as ε_b^I. From the Euler–Bernoulli beam theory, the distribution of normal strain along the thickness direction is calculated by $\varepsilon^I(y) = \varepsilon_b^I + \kappa^I y$. Based on equations (6), (26) and (27), the stresses in SMP and elastomer layers are obtained as

$$\sigma_S^I(y) = \underbrace{[E_S(T_H) - E_S(T_L)]\cdot\varepsilon_0^I - E_S(T_L)\sum_{i=1}^n\triangle\varepsilon_i^I + \sum_{i=1}^n[E_S(T_i)(\triangle\varepsilon_i^I - \alpha_S\triangle T_i)]}_{a_S^I} + \underbrace{E_S(T_L)}_{b_S^I}(\varepsilon_b^I + \kappa^I y), \tag{30}$$

and

$$\sigma_E^I(y) = \underbrace{E_E\alpha_E(T_0 - T_n)}_{a_E^I} + \underbrace{E_E}_{b_E^I}(\varepsilon_b^I + \kappa^I y). \tag{31}$$

Since no external constraint is applied on the composite, both the external force and external moment are equal to 0:

$$\begin{cases} \sum F^I = \int_0^w\int_{\frac{h}{2}-h_S^I}^{\frac{h}{2}}\sigma_S^I(y)dydx + \int_0^w\int_{-\frac{h}{2}}^{\frac{h}{2}-h_S^I}\sigma_E^I(y)dydx = 0 \\ \sum M^I = \int_0^w\int_{\frac{h}{2}-h_S^I}^{\frac{h}{2}}\sigma_S^I(y)ydydx + \int_0^w\int_{-\frac{h}{2}}^{\frac{h}{2}-h_S^I}\sigma_E^I(y)ydydx = 0 \end{cases}. \tag{32}$$

By substituting equations (30) and (31) into equation (32), the curvature κ^I and mid-plane strain ε_b^I can be solved from

$$\begin{Bmatrix}\varepsilon_b^I \\ \kappa^I\end{Bmatrix} = \begin{bmatrix}A^I & B^I \\ B^I & D^I\end{bmatrix}^{-1}\begin{Bmatrix}N_t^I \\ M_t^I\end{Bmatrix}, \tag{33}$$

where $A^I = b_S^I h_S^I + b_E^I h_E^I$,

$$B^I = (b_S^I - b_E^I)h_S^I h_E^I/2,$$
$$D^I = b_S^I[(h/2)^3 - (h/2 - h_S^I)^3]/3 + b_E^I[(h/2 - h_S^I)^3 + (h/2)^3]/3,$$
$$N_t^I = -a_S^I h_S^I - a_E^I h_E^I,$$
$$M_t^I = (a_E^I - a_S^I)h_S^I h_E^I/2.$$

Accordingly, the bending angel θ_1 is obtained by $\theta_1 = \kappa^I L_1$.

Since the laminate in segment 2 bends towards the opposite direction of segment 1, the strain distribution is rewritten as $\varepsilon^{II}(y) = \varepsilon_b^{II} - \kappa^{II} y$. Following the similar procedure, the bending curvature κ^{II} and bending angle θ_2 are obtained. Particularly for the case of $L_2 = 0$, the composite shown in figure 5(a) reduces to a single bilayer laminate.

5.2. Comparison between prediction and experiment

In order to validate the analytical solutions in section 5.1, the active bending behaviors of 3D printed composites were

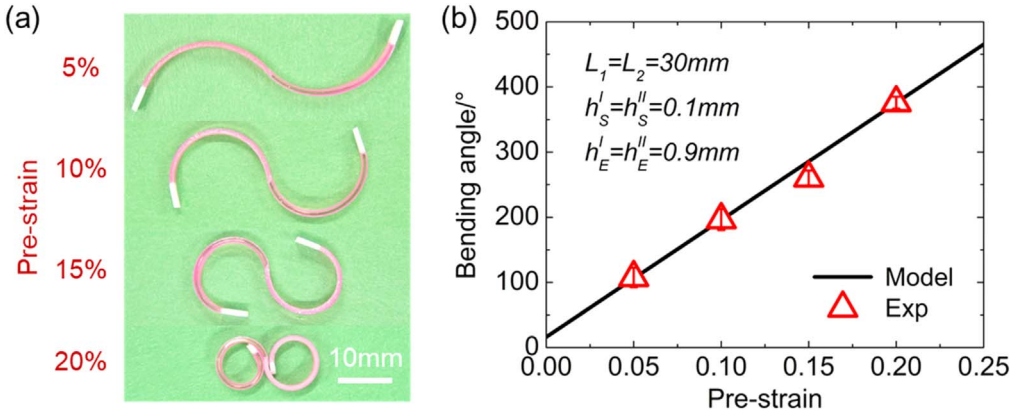

Figure 7. (a) Bending configurations of alternately arranged Vero/Tango (thickness ratio 1:9) bilayer laminates (dimension: 60 mm × 5 mm × 1 mm) under elevated initial strain. The pitch length is 30 mm. (b) Theoretical predictions and experimental results of the bending angle under elevated initial strain.

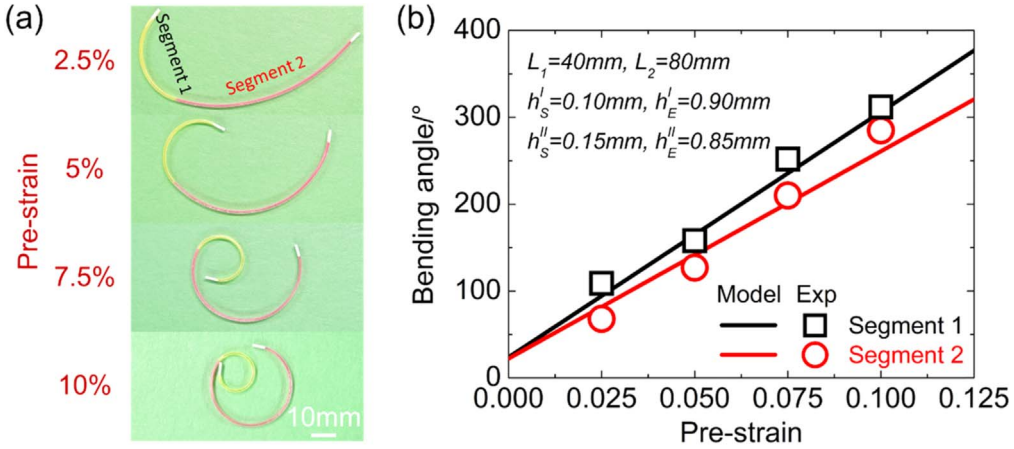

Figure 8. (a) Bending configurations of double segment bilayer laminates (dimension: 120 mm × 5 mm × 1 mm) under elevated initial strain. (segment 1: pitch length is 40 mm; thickness ratio between Vero and Tango is 1:9. segment 2: pitch length is 80 mm; thickness ratio between Vero and Tango is 3:17) (b) Theoretical predictions and experimental results of the bending angle for Segment 1 and 2 under elevated initial strain.

tested under the aforementioned thermomechanical programming process. The experiments were performed in the circulating water bath (Huber CC-118A, Peter Huber Kältemaschinenbau, Offenburg, Germany) with precise temperature control. Herein, the high temperature T_H and low temperature T_L were respectively set as 80 °C and 30 °C.

First, single bilayer laminates (dimension: 60 mm × 5 mm × 1 mm) of different thickness ratios between SMP and elastomer were printed and tested under elevated programming strain from 5% to 20%. Figure 6(a) shows the bending configurations for a particular case where the thickness ratio of SMP and elastomer is 1:4. Theoretical predictions and experimental results of the bending curvature under elevated initial strain and different thickness ratio are presented in figure 6(b). It is seen that under a given thickness ratio, bending curvature approximately linearly increases with the initial programming strain. For a given initial strain and laminate thickness, a thicker SMP layer may produce a smaller bending curvature. This is because a thicker SMP or smaller programming strain may weaken the strain mismatch between the SMP and elastomer layer, and therefore produce a smaller bending curvature. Moreover, the tested curvatures are well captured by the analytical solutions derived in section 5.1. By virtue of the reasonable simplifications, the phase evolution model is also effective in predicting the mechanical behavior of composite structures where SMP plays an important role. Herein, we note that in addition to the geometric parameters and initial strain, the low temperature T_L may also affect the bending curvature of the bilayer laminate. By decreasing T_L, the SMP layer may become too stiff to be pulled by the elastomer layer with a shrinkage tendency, which accordingly yields a smaller bending curvature. More experimental characterizations with lower T_L could be found in the supplementary materials.

Then we further employ the above single bilayer laminate as a building block to realize other complicated deformed configurations. As shown in figure 7(a), two identical bilayer laminates (dimension: 30 mm × 5 mm × 1 mm, thickness ratio between Vero and Tango is 1:9) were designed to be alternately arranged in series to achieve the wavy configuration. Similarly, with the increase of the programming strain, bending angle is gradually increased. Moreover, since the two

Table 2. Comparison between this work and other related works.

	Representative work	Description of material anisotropy	Number of model parameters	Basic material test	Parameter identification method	Availability of analytical solution
Multi-branch thermo-viscoelastic model	[11]	No	17 (table 2 in [11])	1. DMA tests; 2. Uniaxial tension tests; 3. Thermal strain tests; 4. Stress relaxation tests	Fitting the master curve of relaxation modulus	Iterative method is required based on the Boltzmann superposition principle and no analytical solution can be derived. (Refer to equation (10) in [11])
	[8]	No	62 (Table S1 in [8])	1. DMA tests; 2. Thermal strain tests	Fitting the storage modulus and loss factor (tanδ) curves with nonlinear regression (NLREG) method	
Phase evolution model	[41]	Yes	7 for isotropic assumption and 27 for anisotropic assumption(data source: table 1 and equation (33) in [3])	1. DMA tests; 2.Uniaxial tension tests; 3. Thermal strain tests	Fitting the storage modulus curve	Closed form solutions are available. (Refer to equations (14) and (33) in [3])
	This work	No	13 (table 1 in this work)	1. Uniaxial tension tests; 2. Thermal strain tests	Directly obtained from uniaxial tension tests without curve fitting	Explicit analytical solutions are available. (Refer to equations (13)–(20) for pure SMP and equations (30)–(33) for bilayer laminate)

segments are antisymmetric and possess the same stiffness, we can use the calculated curvatures shown in figure 6(b) to directly obtain the corresponding bending angles with $\theta = \kappa L$, where θ is the bending angle and L is the segment length. Again, the theoretical predictions agree well with the experimental results (figure 7(b)).

At last, we demonstrate the helical configurations realized by the double segment bilayer laminate design. In order to achieve helical shape, the bending curvature should be carefully designed otherwise the two ends of the strip may collide to constrain the target deformation. Therefore, each segment is assigned with a specific pitch length and thickness ratio to yield the prescribed bending angles. To achieve a greater bending angle, segment 1 is designed with a pitch length of 40 mm, Vero thickness of 0.1 mm and Tango thickness of 0.9 mm. On the contrary, a smaller bending angle is expected for segment 2 with a larger pitch length (80 mm), thicker Vero thickness (0.15 mm) and thinner Tango thickness (0.85 mm). Figure 8(a) presents the bending configurations of double segment bilayer laminates (dimension: 120 mm × 5 mm × 1 mm) under elevated initial strain. By increasing the programming strain from 2.5% to 10%, the strip bends from a spoon-like shape to helical shape. Moreover, as shown in figure 8(b), the actual bending angles of both segments quantitatively match our theoretical predictions, which proves the feasibility of employing the phase evolution model in the area of structure design.

6. Discussion

Since many other constitutive models for SMP have been developed before this work, it is of vital importance to clarify the differences and advantages of this work in comparison with others.

First, we note that the original motivation of this work is to develop a concise and practical theoretical framework for the 4D printing designers without a vast store of knowledge on solid mechanics and macromolecular physics. Accordingly, without introducing large amount of variables to elaborate chain mobility or entropy variation during SM behavior, we phenomenologically model the glass transition behavior as the evolution (formation or vanishment) of glassy phases to capture the modulus variation in response to temperature.

Before this work, the most popular SMP constitutive model used in the 4D printing area is the multi-branch thermoviscoelastic model. Many representative works in the 4D printing area [8, 11] have adopted this model to conduct the theoretical predictions. Table 2 shows a comparison to elaborate the conciseness of our model in predicting the shape morphing behavior of 4D-printed laminated design.

To be specific, without losing the power of predicting the SM behavior, our model shows its advantage in two aspect. First, the thermoviscoelastic model requires a great number of material parameters and the parameter-fitting process is relatively complicated and laboursome. In this work, on the contrary, no curve fitting is required since all the unknown model parameters can be directly determined from basic material tests.

Second, due to the requirement of computationally inefficient iterative method in problem solving, it is not available to derive closed-form analytical solutions with the thermoviscoelastic model. On the contrary, due to the conciseness of our current model, closed-form analytical solutions can be derived without obvious difficulty to predict the shape evolving behavior of complex 4D-printed structures induced by SM effect, which proves the wide applicability of our model.

Finally, we compare our model with another phenomenological model proposed by Bodaghi *et al* [41] which not only provides the analytical closed-form solutions to replicate thermo-mechanical behaviors of SMPs but also considers the effect of the 3D printing-induced material anisotropy with minimum experimentally characterized parameters. In that model, the rubbery and glassy phases are arranged in series and the concept of 'stored inelastic strain' is employed to characterize the phase transformation occurred in SMP. The model is then used to predict the reheating caused sequential recovery of the multi-SMP laminate. From the perspective of mechanics modeling, the model presented in [41] is precise and robust enough to predict the mechanical behavior of SMP in most of the working conditions. However, the relatively complicated mathematical expressions in tensor form make this model challenging for those 4D printing designers who do not have strong background in solids mechanics to understand and implement into specific applications. In comparison, our model provides the analytical solutions in a mathematically readable form to help the 4D printing designers predict and optimize the temporarily fixed shapes at low temperature. The mathematical conciseness makes our model readily implemented into engineering designs with complex geometry. Moreover, in our model, the rubbery phase and multiple glassy phases are arranged in parallel, and the formation of new glassy phases and vanishment of existing glassy phases are respectively characterized by using the 'temperature-controlled switches' concept. We notice that the demonstrations of 4D printed bilayer composites in this work are similar to the previously reported demonstrations [11, 14, 41]. We acknowledge the novelty of the previous report, and use these demonstrations in this work only for the purpose of validating the accuracy and applicability of our proposed model.

7. Conclusion

In this paper, a simplified phenomenological model is developed to describe the glass transition behavior of SMP where the concept of phase evolution is retained. Explicit iterative formats of the stress–strain relationship are respectively presented for the phase generation and vanishment process. Its inherent conciseness allows the model to provide closed-form analytical solutions of SM behavior for pure SMP or SMP based composite structures. Accuracy of the predictions is verified by the good agreement with the

corresponding experiments. Furthermore, in addition to provide effective assistance in SM-based 4D printing design, the model is promising to be expanded into other soft materials with analogous phase evolution characteristics.

Acknowledgments

We gratefully acknowledge the grant (RGDM1710205) from SUTD Digital Manufacturing and Design Centre (DManD) funded by the Singapore National Research Foundation. F W acknowledges the support by the NSFC (No. 11802233). Q G acknowledges the research startup grant (Y01336121) by Shenzhen municipal government and the research startup grant (Y01336221) support by Southern University of Science and Technology. Q G also acknowledges the support by the Centers for Mechanical Engineering Research and Education at MIT and SUSTech.

ORCID iDs

Qi Ge https://orcid.org/0000-0002-8666-8532

References

[1] Raviv D *et al* 2014 Active printed materials for complex self-evolving deformations *Sci. Rep.* **4** 7422
[2] Kuang X, Roach D J, Wu J T, Hamel C M, Ding Z, Wang T J, Dunn M L and Qi H J 2019 Advances in 4D printing: materials and applications *Adv. Funct. Mater.* **29** 1805290
[3] Ge Q, Qi H J and Dunn M L 2013 Active materials by four-dimension printing *Appl. Phys. Lett.* **103** 131901
[4] Saed M O *et al* 2019 Molecularly-engineered, 4D-printed liquid crystal elastomer actuators *Adv. Funct. Mater.* **29** 1806412
[5] Huang L M, Jiang R Q, Wu J J, Song J Z, Bai H, Li B G, Zhao Q and Xie T 2017 Ultrafast digital printing toward 4D shape changing materials *Adv. Mater.* **29** 1605390
[6] Kuang X, Wu J T, Chen K J, Zhao Z, Ding Z, Hu F J Y, Fang D N and Qi H J 2019 Grayscale digital light processing 3D printing for highly functionally graded materials *Sci. Adv.* **5** eaav5790
[7] Ge Q, Sakhaei A H, Lee H, Dunn C K, Fang N X and Dunn M L 2016 Multimaterial 4D printing with tailorable shape memory polymers *Sci. Rep.* **6** 31110
[8] Ding Z, Yuan C, Peng X R, Wang T J, Qi H J and Dunn M L 2017 Direct 4D printing via active composite materials *Sci. Adv.* **3** e1602890
[9] Kim Y, Yuk H, Zhao R K, Chester S A and Zhao X H 2018 Printing ferromagnetic domains for untethered fast-transforming soft materials *Nature* **558** 274–9
[10] Liu G, Zhao Y, Wu G and Lu J 2018 Origami and 4D printing of elastomer-derived ceramic structures *Sci. Adv.* **4** eaat0641
[11] Ge Q, Dunn C K, Qi H J and Dunn M L 2014 Active origami by 4D printing *Smart Mater. Struct.* **23** 094007
[12] Gladman A S, Matsumoto E A, Nuzzo R G, Mahadevan L and Lewis J A 2016 Biomimetic 4D printing *Nat. Mater.* **15** 413–8
[13] Mao Y Q, Ding Z, Yuan C, Ai S G, Isakov M, Wu J T, Wang T J, Dunn M L and Qi H J 2016 3D printed reversible shape changing components with stimuli responsive materials *Sci. Rep.* **6** 24761
[14] Wu J T, Yuan C, Ding Z, Isakov M, Mao Y Q, Wang T J, Dunn M L and Qi H J 2016 Multi-shape active composites by 3D printing of digital shape memory polymers *Sci. Rep.* **6** 24224
[15] Zhang Q, Zhang K and Hu G K 2016 Smart three-dimensional lightweight structure triggered from a thin composite sheet via 3D printing technique *Sci. Rep.* **6** 22431
[16] Yuan C, Wang T J, Dunn M L and Qi H J 2017 3D printed active origami with complicated folding patterns *Int. J. Precis. Eng. Manuf.-Green. Technol.* **4** 281–9
[17] Yuan C, Ding Z, Wang T J, Dunn M L and Qi H J 2017 Shape forming by thermal expansion mismatch and shape memory locking in polymer/elastomer laminates *Smart Mater. Struct.* **26** 105027
[18] Akbari S, Sakhaei A H, Kowsari K, Yang B, Serjouei A, Zhang Y F and Qi G 2018 Enhanced multimaterial 4D printing with active hinges *Smart Mater. Struct.* **27** 065027
[19] Zhang Y F, Zhang N B, Hingorani H, Ding N Y, Wang D, Yuan C, Zhang B, Gu G Y and Ge Q 2019 Fast-response, stiffness-tunable soft actuator by hybrid multimaterial 3D printing *Adv. Funct. Mater.* **29** 1806698
[20] Ge Q, Yu K, Ding Y and Jerry Q H 2012 Prediction of temperature-dependent free recovery behaviors of amorphous shape memory polymers *Soft Matter* **8** 11098–105
[21] Yu K, Ge Q and Qi H J 2014 Reduced time as a unified parameter determining fixity and free recovery of shape memory polymers *Nat. Commun.* **5** 3066
[22] Ge Q, Luo X, Rodriguez E D, Zhang X, Mather P T, Dunn M L and Qi H J 2012 Thermomechanical behavior of shape memory elastomeric composites *J. Mech. Phys. Solids* **60** 67–83
[23] Ge Q, Serjouei A, Qi H J and Dunn M L 2016 Thermomechanics of printed anisotropic shape memory elastomeric composites *Int. J. Solids Struct.* **102** 186–99
[24] Behl M and Lendlein A 2007 Shape-memory polymers *Mater. Today* **10** 20–8
[25] Zhao Q, Qi H J and Xie T 2015 Recent progress in shape memory polymer: new behavior, enabling materials, and mechanistic understanding *Prog. Polym. Sci.* **49–50** 79–120
[26] Leng J S, Lan X, Liu Y J and Du S Y 2011 Shape-memory polymers and their composites: stimulus methods and applications *Prog. Mater Sci.* **56** 1077–135
[27] Diani J, Gilormini P, Frédy C and Rousseau I 2012 Predicting thermal shape memory of crosslinked polymer networks from linear viscoelasticity *Int. J. Solids Struct.* **49** 793–9
[28] Nguyen T, Qi H J, Castro F and Long K 2008 A thermoviscoelastic model for amorphous shape memory polymers: incorporating structural and stress relaxation *J. Mech. Phys. Solids* **56** 2792–814
[29] Nguyen T D, Yakacki C M, Brahmbhatt P D and Chambers M L 2010 Modeling the relaxation mechanisms of amorphous shape memory polymers *Adv. Mater.* **22** 3411–23
[30] Xiao R, Choi J, Lakhera N, Yakacki C M, Frick C P and Nguyen T D 2013 Modeling the glass transition of amorphous networks for shape-memory behavior *J. Mech. Phys. Solids* **61** 1612–35
[31] Yu K, Xie T, Leng J, Ding Y and Qi H J 2012 Mechanisms of multi-shape memory effects and associated energy release in shape memory polymers *Soft Matter* **8** 5687–95
[32] Westbrook K K, Kao P H, Castro F, Ding Y F and Qi H J 2011 A 3D finite deformation constitutive model for amorphous shape memory polymers: a multi-branch modeling approach

for nonequilibrium relaxation processes *Mech. Mater.* **43** 853–69

[33] Gilormini P and Diani J 2012 On modeling shape memory polymers as thermoelastic two-phase composite materials *CR Mec.* **340** 338–48

[34] Liu Y, Gall K, Dunn M L, Greenberg A R and Diani J 2006 Thermomechanics of shape memory polymers: uniaxial experiments and constitutive modeling *Int. J. Plast.* **22** 279–313

[35] Long K N, Dunn M L and Qi H J 2010 Mechanics of soft active materials with phase evolution *Int. J. Plast.* **26** 603–16

[36] Qi H J, Nguyen T D, Castro F, Yakacki C M and Shandas R 2008 Finite deformation thermo-mechanical behavior of thermally induced shape memory polymers *J. Mech. Phys. Solids* **56** 1730–51

[37] Reese S, Böl M and Christ D 2010 Finite element-based multi-phase modelling of shape memory polymer stents *Comput. Method Appl. Mech.* **199** 1276–86

[38] Lu H B, Wang X D, Yao Y T and Fu Y Q 2018 A 'frozen volume' transition model and working mechanism for the shape memory effect in amorphous polymers *Smart Mater. Struct.* **27** 065023

[39] Ding Z, Weeger O, Qi H J and Dunn M L 2018 4D rods: 3D structures via programmable 1D composite rods *Mater. Des.* **137** 256–65

[40] Sundaram S, Kim D S, Baldo M A, Hayward R C and Matusikt W 2017 3D-printed self-folding electronics *ACS Appl. Mater. Inter.* **9** 32290–8

[41] Bodaghi M, Damanpack A R and Liao W H 2016 Self-expanding/shrinking structures by 4D printing *Smart Mater. Struct.* **25** 105034